Biomaterials Science

PAPER

View Article Online
View Journal | View Issue

Published on 25 September 2014. Downloaded by Izmir Yuksek Teknoloji on 22/05/2017 11:50:19.

Cite this: *Biomater. Sci.*, 2015, **3**, 323

The endocytic pathway and therapeutic efficiency of doxorubicin conjugated cholesterol-derived polymers†

Sema Sevimli,[a,b,c] Sharon Sagnella,[b,c] Alexander Macmillan,[c] Renee Whan,[c] Maria Kavallaris,[b,c] Volga Bulmus[d] and Thomas P. Davis*[e,f]

Received 18th June 2014,
Accepted 15th September 2014

DOI: 10.1039/c4bm00224e

www.rsc.org/biomaterialsscience

Previously synthesized poly(methacrylic acid-*co*-cholesteryl methacrylate) P(MAA-*co*-CMA) copolymers were examined as potential drug delivery vehicles. P(MAA-*co*-CMA) copolymers were fluorescently labelled and imaged in SHEP and HepG2 cells. To understand their cell internalization pathway endocytic inhibition studies were conducted. It was concluded that P(MAA-*co*-CMA) are taken up by the cells *via* clathrin-independent endocytosis (CIE) (both caveolae mediated and cholesterol dependent endocytosis) mechanisms. The formation and characterization of P(MAA-*co*-CMA)–doxorubicin (DOX) nanocomplexes was investigated by fluorescence lifetime imaging microscopy (FLIM), UV-Visible spectroscopy (UV-Vis) and dynamic light scattering (DLS) studies. The toxicity screening between P(MAA-*co*-CMA)–DOX nanocomplexes (at varying w/w ratios) and free DOX, revealed nanocomplexes to exhibit higher cytotoxicity towards cancer cells in comparison to normal cells. FLIM and confocal microscopy were employed for investigating the time-dependent release of DOX in SHEP cells and the cellular uptake profile of P(MAA-*co*-CMA)–DOX nanocomplexes in cancer and normal cell lines, respectively. The endocytic pathway of P(MAA-*co*-CMA)–DOX nanocomplexes were examined in SHEP and HepG2 cells *via* flow cytometry revealing the complexes to be internalized through both clathrin-dependent (CDE) and CIE mechanisms. The drug delivery profile, reported herein, illuminates the specific endocytic route and therapeutic efficiency of P(MAA-*co*-CMA)–DOX nanocomplexes strongly suggesting these particles to be promising candidates for *in vivo* applications.

Introduction

Advanced drug delivery systems aim to enhance the efficacy of traditional medicine by introducing new therapeutic strategies. The moment a therapeutic is injected into the body, its medicinal effect is somewhat hindered due to rapid elimination triggered by renal excretion and/or hepatic metabolism; which restricts the effective dose reaching the target sites. During drug circulation throughout the body, accumulation at off-target sites can cause toxicity leading to unwanted side effects.[1] Characteristic properties seen at target sites such as pH and temperature gradients, the presence of specific enzymes and receptors have been taken into account in the process of designing delivery systems to overcome the non-specific delivery issues.[2–6] Nano-sized polymers containing therapeutic entities like drugs, genes or peptides – with enhanced targeted-delivery properties – have been established as a credible option for clinical development. These nano-scaled delivery vehicles offer significant advantages as they enhance therapeutic efficiency by prolonging drug half-life, improving solubility of hydrophobic entities, reducing

[a]*The Centre for Advanced Macromolecular Design (CAMD), The University of New South Wales, Sydney, New South Wales 2052, Australia*
[b]*Australian Centre for Nanomedicine (ACN), The University of New South Wales, Sydney, New South Wales 2052, Australia*
[c]*Children's Cancer Institute Australia (CCIA), Lowy Cancer Research Centre, The University of New South Wales, Sydney, New South Wales 2052, Australia*
[d]*Department of Chemical Engineering, Biotechnology and Bioengineering Graduate Program, Izmir Institute of Technology, Urla, Izmir 35430, Turkey*
[e]*ARC Centre of Excellence in Convergent Bio-Nano Science & Technology, Monash Institute of Pharmaceutical Sciences, Monash University, Parkville, Melbourne, Victoria 3052, Australia. E-mail: Thomas.P.Davis@monash.edu; Tel: +61 3 9903 9260*
[f]*Department of Chemistry, University of Warwick, Coventry, West Midlands CV4 7AL, UK*

†Electronic supplementary information (ESI) available: Intracellular distributions of endocytic markers in SHEP and HepG2 cell lines, toxicity screening of DOX and P(MAA-*co*-CMA)-DOX nanocomplexes at varying complexation ratios in SHEP, HepG2 and MRC5 cells, FLIM analysis of P(MAA-*co*-CMA)-DOX nanocomplexation overtime, live cell imaging of DOX and P(MAA-*co*-CMA)-DOX nanocomplexes in HepG2 and MRC5 cells at different time points, endocytic inhibition studies of P(MAA-*co*-CMA)-DOX nanocomplexes in SHEP cells studies by confocal microscopy; Fig. S1–S8, the formation of stable amide bonds and schematic representation of a phasor plot; Schemes S1–S2. See DOI: 10.1039/c4bm00224e

Published on 25 September 2014. Downloaded by Izmir Yuksek Teknoloji on 22/05/2017 11:50:19.

potential immunogenicity, and/or releasing therapeutics in a sustained or stimuli-triggered manner.[7] Since the structure of polymer carriers greatly influences the bioactivity of their therapeutic cargos, an in depth understanding of cellular processing and uptake mechanisms of polymer-drug complexes will elucidate the rational design of polymers as effective drug delivery systems.[8,9]

Endocytosis – a naturally occurring membrane-bound internalization process observed in all cells – is responsible for the uptake of polymer carriers.[10,11] Based on the size and material of the load, endocytosis can occur by different mechanisms; (1) phagocytosis: the uptake of solid large particles specific to neutrophils and macrophages[12] and (2) pinocytosis: known as fluid and solute-phase endocytosis which transpires *via* macropinocytosis (internalizes particles up to 5 μm in size), clathrin-dependent (CDE) (up to 200 nm in size) or clathrin-independent (CIE) endocytosis.[10,13,14] Cholesterol-dependent and caveolae-mediated pathways are subdivisions of CIE. Caveolae (50-80 nm) are cholesterol and glycosphingolipid rich microdomains on the cell membrane which are involved in cholesterol homeostasis and glycosphingolipid transport.[15]

Doxorubicin (DOX), a chemotherapeutic agent, has been utilized in the treatment of various cancers including breast, lung, multiple myeloma and lymphoma.[16] While highly effective, this well-known antitumor drug is associated with challenges such as those caused by dose-limiting toxicity, resistance mechanisms developed in cancer cells thereby reducing drug uptake and cardiotoxicity.[17] One of the many approaches to overcome these limitations and enhance the efficacy of DOX is by utilizing polymers as drug carriers. Various polyanions such as polyglutamate;[18] polyaspartate,[19] poly(acrylic acid),[20,21] γ-polyglutamic acid,[22] block ionomers of aspartate, benzyl glutamate[23] and benzyl aspartate[24] with poly(ethylene oxide) have demonstrated encouraging results in terms of binding and delivering DOX into targeted cells and tissues. Consequently, anionic poly(methacrylic acid-*co*-cholesteryl methacrylate) P(MAA-*co*-CMA) copolymer series – comprised of enriched electrostatic binding abilities and pH-responsive/membrane disruptive properties – were investigated as potential DOX carriers.

The present study focuses on the ability of cholesterol-derived ionic copolymers to effectively deliver DOX while controlling its endocytic mechanism, enhancing its efficacy (*vs.* free drug) in carcinoma cells and limiting its toxicity towards normal cell lines, thereby overcoming one of the major obstacles seen in advanced drug delivery systems. Accordingly, the specific cell uptake profile and drug delivery efficiency of P(MAA-*co*-CMA) copolymers (with varying CMA units) were evaluated in carcinoma and normal cells. The physicochemical properties – such as charge, size and toxicity profile – of P(MAA-*co*-CMA)–DOX nanocomplexes as well as their therapeutic efficacy were evaluated. The cellular internalization mechanism of both polymers and nanocomplexes were assessed in terms of determining their specific endocytic route *via* flow cytometry and living cell confocal microscopy.

Results and discussion

Modification and fluorescent labelling of P(MAA-*co*-CMA)

To visualize the cellular internalization profile of both the copolymers and nanocomplexes; P(MAA-*co*-CMA) copolymer series were fluorescently tagged with Alexa Fluor® 488. The carboxylate groups on P(MAA-*co*-CMA) were tailored into stable amide bonds prior to chemical labelling applications. 2 mol% of the carboxylate groups on each P(MAA-*co*-CMA) sample was targeted and modified according to the protocol described in literature.[25] Carboxylates were reacted with *N*-hydroxysulfosuccinimide (NHS-sulfo) in the presence of ethyl (dimethylaminopropyl) carbodiimide (EDC), resulting in a semi-stable NHS-sulfo ester intermediate. The amine-reactive NHS ester groups were then reacted with cystamine dihydrochloride forming a stable amide bond (Scheme S1, ESI†). This modification was characterized *via* H^1 NMR and FTIR spectroscopy; however the NMR spectrum failed to illustrate the chemical-bond changes in the polymer due to the overlapping broad-D_2O peak. Alternatively, FTIR spectroscopy revealed alterations in the polymer structure as indicated by a significant reduction in the intensity of the distinctive carboxylic acid O–H (3400–2900 cm^{-1}) and C═O (1630–1550 cm^{-1}) stretch and the appearance of peaks between 1650–1580 (N–H bend) and 1020-1220 (aliphatic amines) (Fig. 1-A).

The modified polymer was then labelled with the fluorescent maleimide dye, Alexa Fluor® 488. The Beer–Lambert Law ($A = \varepsilon \times b \times C$; where A is the absorbance, ε is extinction coefficient ($M\ cm^{-1}$), b is wavelength (cm) and C is the concentration (M)) was employed for calculating the final fluorescent dye content on each polymer *via* UV-Visible spectroscopy. The extinction coefficient (ε) for each copolymer (at 275 nm specific for cholesterol, in MilliQ water) was obtained from a calibration curve of standard P(MAA-*co*-CMA) solutions in MilliQ water (Fig. 1-B). Using the ε values of copolymers and Alexa Fluor® 488 dye (ε = 71 000 $M\ cm^{-1}$) the final concentrations of both components in the modified structure were calculated. The Alexa Flour dye content of 8 mol% CMA-modified copolymer was found to be 0.22 mol%; which is sufficient for effective detection by confocal microscopy analysis.[26]

The internalization profile of P(MAA-*co*-CMA)

Confocal laser scanning microscopy was employed to visualize the cell uptake profile of the P(MAA-*co*-CMA) copolymer series in both human neuroblastoma (SHEP) and human liver hepatocellular carcinoma (HepG2) cell lines. HepG2 cells were selected due to their well-known cholesterol recognition profile.[27] Cholesterol-based systems have been heavily investigated in the liver[28] and liver cells,[29,30] where they have shown encouraging results. SHEP and HepG2 cells were treated with 2 $\mu g\ ml^{-1}$ of Alexa Fluor 488 labelled P(MAA-*co*-CMA) copolymer series for 1 hour. As seen in Fig. 2, representative Alexa Fluor 488 labelled 8 mol% CMA copolymers were readily taken up by both cell lines localizing in the cytoplasm. In line with previous findings, cell internalization of P(MAA-*co*-CMA) copolymers is influenced by their hydrophobicity (internalization

 This journal is © The Royal Society of Chemistry 2015

Published on 25 September 2014. Downloaded by Izmir Yuksek Teknoloji on 22/05/2017 11:50:19.

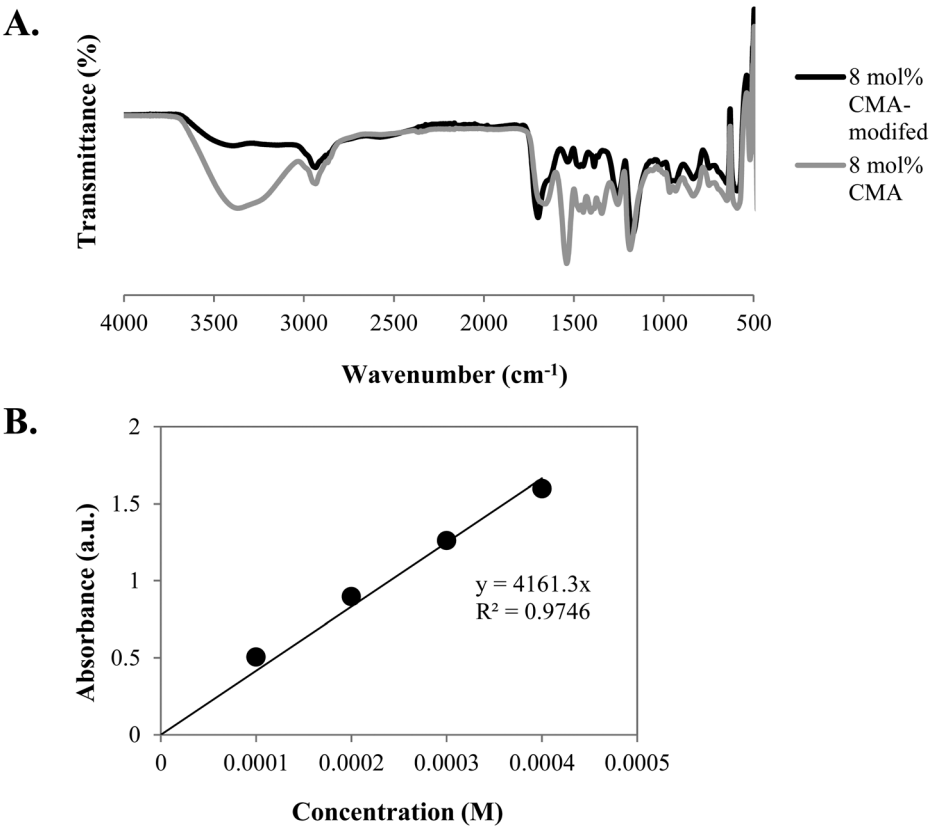

Fig. 1 (A) ATR-FTIR spectrums of 8 mol% CMA (grey) and 8 mol% CMA-modified (black) copolymers. (B) UV absorption of standard solutions prepared with 8 mol% CMA in MilliQ water (at 275 nm).

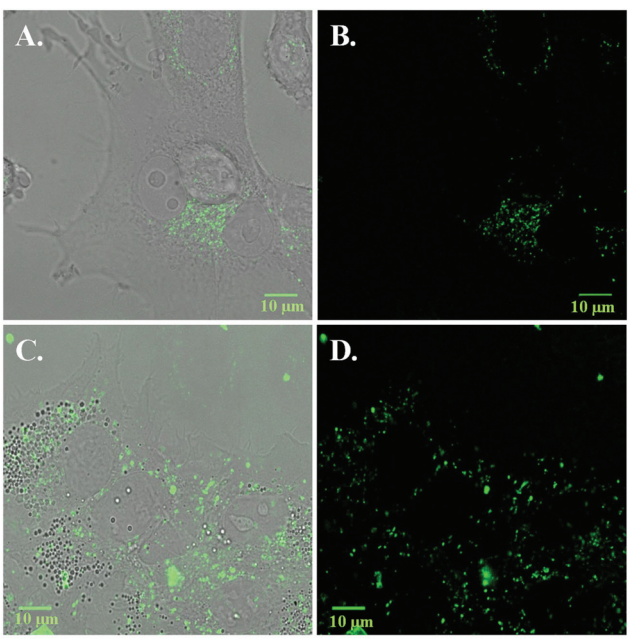

Fig. 2 Confocal microscopy images of (A–B) SHEP and (C–D) HepG2 cells treated with Alexa Fluor 488 labelled 8 mol% CMA copolymers (2 μg ml^{-1}) in serum media for 1 hour. Alexa Fluor 488 (λ^{ex} = 495 nm and λ^{em} = 591 nm) was excited using a 485 nm laser. Scale bars correspond to 10 μm.

increases with higher CMA units).[31] It should be noted that the internalization process of P(MAA-*co*-CMA) copolymers is not in any way influenced by modification/labelling as control flow cytometry studies revealed that both modified and unmodified polymers displayed the same transfection efficacy.

The internalization mechanism of lipid-based systems are believed to be driven by endocytosis.[9] To determine the specific endocytic pathway of P(MAA-*co*-CMA) copolymers, endocytosis inhibition studies were carried out. CDE and CIE endocytosis were the two major pathways evaluated utilizing the common endocytosis inhibitors; chlorpromazine, methyl-β-cyclodextrin (MβCD) and genistein. Chlorpromazine, *an inhibitor for CDE*,[32,33] is a cationic amphiphilic drug which translocates clathrin and its related proteins to intracellular vesicles thus suppressing the formation of clathrin coated pits.[34] Cholesterol-dependent and caveolae-mediated pathways are subdivisions of CIE.[10] MβCD, a cyclic oligomer of glucopyranoside, reversibly removes steroids from the plasma membrane as a result inhibits cholesterol-dependent endocytosis.[35,36] Caveolae-mediated endocytosis was inhibited by a tyrosine-kinase inhibitor, genistein.[37]

A control study investigating the *in vitro* cytotoxicity profile of each inhibitor was performed in both SHEP and HepG2 cells. Results indicated the optimal protocol to be 2 hour treatments of endocytic inhibitors at concentration levels of 5 μg ml^{-1} chlorpromazine, 2.5 mM MβCD and 300 μM genistein.

Published on 25 September 2014. Downloaded by Izmir Yuksek Teknoloji on 22/05/2017 11:50:19.

Following inhibitor toxicity studies, confocal microscopy was employed to assess the specificity of the inhibitors in relation to the uptake of molecules known to taken up by specific endocytic routes, Human transferrin (hTF)[38] and lactosylceramide (LacCer).[39] hTF is known to be taken up *via* CDE while LacCer is internalized *via* CIE where is associated with lipid rafts.[40] Fig. S1 and S2† show the CDE and CIE inhibitors suppressing the hTF and LacCer uptake in SHEP and HepG2 cells, respectively. Treating cells with 5 μg ml^{-1} chlorpromazine 2 hours before hTF addition (Fig. S1-C and S2-C†) reduced the internalization profile of hTF in comparison to control sample (Fig. S1-A and S2-A†). These results displayed the inhibitory effect of chlorpromazine on hTF, verifying its specificity towards CDE along with illuminating the optimal inhibitor conditions (5 μg ml^{-1} chlorpromazine for 2 hours).

Confocal images in Fig. S1-B and S2-B† show the uptake of LacCer molecules into untreated SHEP and HepG2 cells, respectively. Inhibition studies utilizing MβCD at 2.5 mM resulted in a reduction in LacCer internalization into either cell type (Fig. S1-D and S2-D†). Cell blockage was clearly visualized by the distinct green border surrounding the cell walls which implied effective inhibition combined with the reduction in the number of visible vesicles in the cytoplasm. Consistent with previous MβCD treatments, the cell morphologies slightly changed, which was attributed to cholesterol depletion and rearrangement of the cytoskeleton.[41] Based on the cell viability data and confocal images 2.5 mM MβCD for 2 hours was the preferential settings for inhibiting CIE. In accordance with MβCD treatments, genistein *also* blocked LacCer uptake to the cells (Fig. S1-E and S2-E†). Interestingly HepG2 cells showed a higher response to inhibition than SHEP cells, as they changed their morphology while blocking the CIE pathway.

After establishing the ideal inhibitor conditions (cells *versus* concentration) and confirming the specific uptake mechanism for each inhibitor; studies investigating the endocytic pathway of statistical copolymers were subsequently carried out.

Initially, polymer internalization was assessed in correspondence to the CDE uptake mechanism. Confocal images of P(MAA-*co*-CMA) uptake in SHEP and HepG2 cells – pre-treated with chlorpromazine – are shown in Fig. 3(A–B) and 4(A–B), respectively. Results indicate that the polymer internalization mechanism was not affected by chlorpromazine treatments, as they were readily taken up by both cell lines displaying similar uptake profiles to untreated cells (Fig. 2).

Thereafter, investigations followed the involvement of CIE pathways on polymer internalization *via* MβCD and genistein inhibitors. Fig. 3(C–D) and 4(C–D) shows the uptake of copolymers after a 2 hour MβCD treatment. The pre-incubation of MβCD in both cell lines, resulted in inhibitory effects for polymer endocytosis. Owing to the cholesterol moieties, in the copolymer composition, hydrophobic interactions between the plasma membrane and P(MAA-*co*-CMA) were blocked thus preventing cellular internalization from taking place (shown by yellow arrows).

Lastly, the endocytic pathway of polymers was investigated after 300 μM genistein treatments in SHEP and HepG2 cells Fig. 3(E–F) and 4(E–F), respectively. Images indicate that genistein noticeably effects the cellular uptake mechanism of P(MAA-*co*-CMA); as the polymers mostly appear on the surface of plasma membrane (represented by pink arrows).

It is evident from these results that CIE is the main endocytic pathway involved in P(MAA-*co*-CMA) internalization by

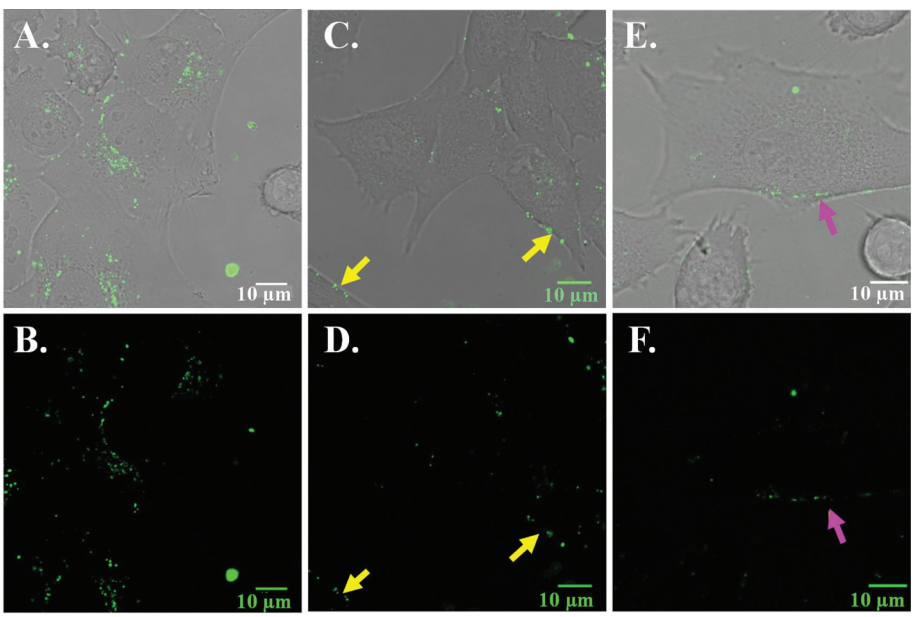

Fig. 3 Evaluation of Alexa Fluor 488 labelled 8 mol% CMA copolymers (2 μg ml^{-1}) uptake in SHEP cells after 2 hour treatments of (A–B) chlorpromazine (5 μg ml^{-1}), (C–D) MβCD (2.5 mM) and (E–F) genistein (300 μM). Alexa Fluor 488 fluorescent images were acquired at λ^{ex} = 495 nm and λ^{em} = 591 nm. Scale bars represent 10 μm.

 This journal is © The Royal Society of Chemistry 2015

Published on 25 September 2014. Downloaded by Izmir Yuksek Teknoloji on 22/05/2017 11:50:19.

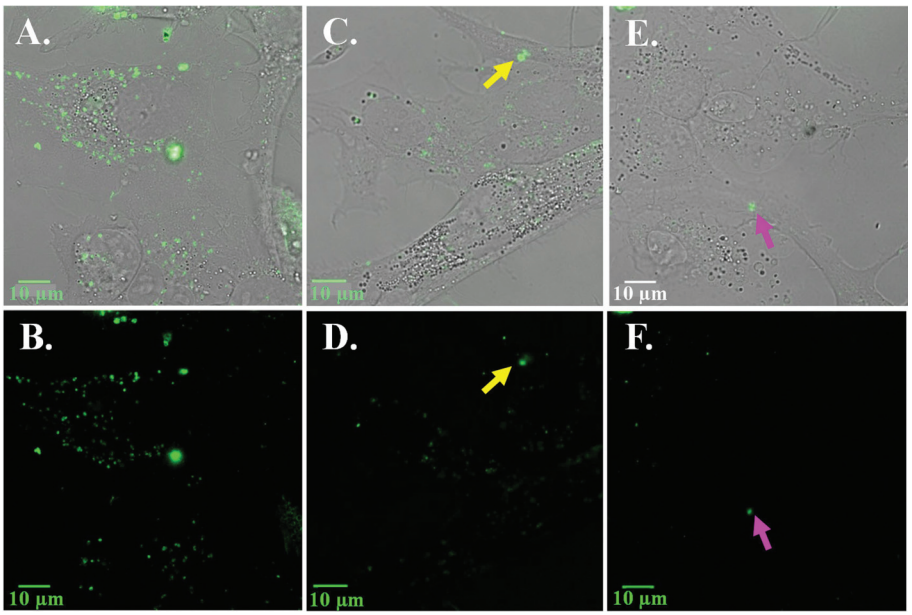

Fig. 4 Intracellular distribution of Alexa Fluor 488 labelled 8 mol% CMA copolymers (2 μg ml^{-1}) after 2 hour treatments of (A–B) chlorpromazine (5 μg ml^{-1}), (C–D) MβCD (2.5 mM) and (E–F) genistein (300 μM) in HepG2 cells. Alexa Fluor 488 (λ^{ex} = 495 nm and λ^{em} = 591 nm) was excited using a 488 nm laser. Scale bars represent 10 μm.

SHEP and HepG2 cells. Polymer uptake was governed solely by their hydrophobic moieties which is very common with lipid-based systems.[10,40–42] It should be mentioned that a preliminary quantitative analysis on inhibitory effects was undertaken by flow cytometry. However, the assay was not feasible as the desired amount of Alexa Fluor labelled polymer, for sufficient detection *via* flow cytometry, was too large to chemically synthesize in a cost-effective and efficient manner.

Characterization studies of P(MAA-*co*-CMA)–DOX nanocomplexes

Upon establishing the cellular internalization profile of P(MAA-*co*-CMA) series, the anionic copolymers were than exploited as potential drug delivery systems. DOX, a cationic anticancer drug,[20,21] encompasses amine groups which bestow cationic properties to the molecule resulting in a pK_a value of 8.6.[43,44] Owing to these positive charges, DOX molecules are predicted to instigate electrostatic interactions between the carboxylic components of P(MAA-*co*-CMA) series (pK_a ~ 5.0)[45] at neutral conditions. Consequently, DOX was selected as a model chemotherapeutic for examining the complexation efficiency to P(MAA-*co*-CMA) series while evaluating the nanocomplexes therapeutic efficacy in a variety of cells.

Fluorescence lifetime imaging microscopy (FLIM) is a useful tool for differentiating free DOX from its polymer conjugated form.[46] The fluorescence lifetimes of unbound DOX and P(MAA-*co*-CMA)–DOX nanocomplexes in aqueous solution were measured *via* time-correlated single photon counting (TCSPC) and represented in a phasor plot.[47,48] The lifetime of each species is categorized in pixel format and transformed into a phasor plot by fitting the data to an exponential decay. All single exponential lifetimes lie on the universal circle while multi-exponential lifetimes are a linear combination of their components (Scheme S2, ESI†).

The phasor plot seen in Fig. 5(A–B) shows the difference in fluorescence lifetime for both free DOX and nanocomplexes prepared at varying w/w ratios at 0 hours. The free DOX exhibits a lifetime of 1 ns[46] and the nanocomplexes at 0 hours display a dominant longer lifetime verifying P(MAA-*co*-CMA)–DOX conjugation as shown by their position in the phasor plot.[49,50]

The data indicated that with increasing P(MAA-*co*-CMA)–DOX nanocomplexation ratios from 125 : 1 to 1250 : 1 longer lifetimes were observed in the same region. The stability of the P(MAA-*co*-CMA)–DOX nanocomplexes (prepared at varying ratios 6.25 : 1–1250 : 1) were further examined over a 24 hour incubation period (Fig. S3, ESI†). The phasor plot shift from free DOX to nanocomplexes (longer lifetime) within the hour confirms steady complexation however loss of stability is observed at 24 hours by the existence of two lifetimes under the exponential decay.

In agreement with the FLIM data, P(MAA-*co*-CMA)–DOX nanocomplexes were prepared in MilliQ water at varying w/w ratios ranging from 6.25 : 1 to 1250 : 1 and were analysed *via* UV-Vis. A representative absorbance spectrum of free DOX along with P(MAA-*co*-CMA)–DOX nanocomplex (6.25 : 1) is displayed in Fig. 5-C. The DOX spectrum illustrates maximum absorbance at 480 nm and 2 shoulders at 500 and 535 nm. P(MAA-*co*-CMA) complexation resulted in a 10 nm bathochromic shift of λ_{max} in the spectrum, overall decreasing the optical density of solution.[21] π–π stacking interactions between the DOX molecules and polymers (immobilizing DOX along the polymer chains) was the reason for bathochromic shift in the absorbance spectrum, which commonly is seen with

Published on 25 September 2014. Downloaded by Izmir Yuksek Teknoloji on 22/05/2017 11:50:19.

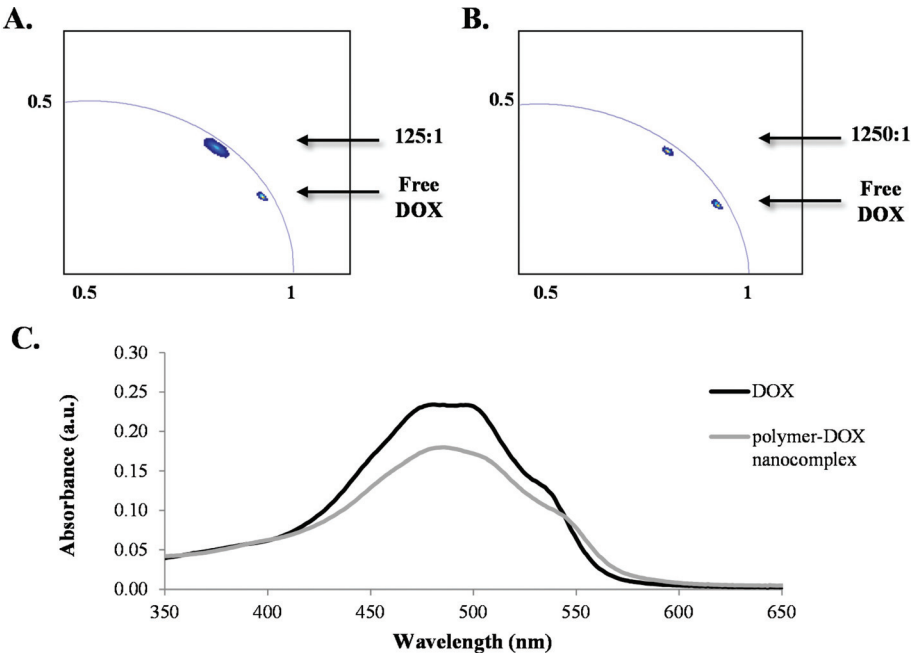

Fig. 5 Phasor analysis for P(MAA-*co*-CMA)–DOX nanocomplexes at (A) 125 : 1 and (B) 1250 : 1 (w/w) ratios at 0 hours. 1.4 μM free DOX was included as a control sample. (C) UV-Visible spectrum of free DOX and P(MAA-*co*-CMA)–DOX nanocomplex in MilliQ water at 480 nm.

chromophore–polyelectrolyte conjugates evidencing complex formation.[20,51,52]

The structure of DOX encompasses an aglycone moiety, *a tetracyclic chromophore where the aromatic rings form a planar anthraquinone system*, which is attached to an amino sugar daunosamine through glycosidic bonds. The complexation reactions are believed to be driven by a number of forces including ionic interactions (mentioned in the previous section), hydrogen bonding and π–π stacking interactions. Hydrogen bonding is formed amongst the hydroxyl groups attached to the anthraquinone ring in DOX and hydroxyl groups of polymer. π–π stacking interactions are facilitated by the aromatic rings, in the anthraquinone system, which are the driving forces of intercalating DNA.[51]

Accordingly P(MAA-*co*-CMA)–DOX nanocomplexes were prepared at w/w ratios of 6.25 : 1, 125 : 1 and 1250 : 1 in MilliQ water. The hydrodynamic diameter, polydispersity index and ζ-potential of the complexes were determined by DLS studies (Table 1). Complexes prepared with increasing polymer ratios displayed a reduction in their effective diameter. Proportional to the increase of substitutes in the complex, enhancements in inter/intramolecular forces are *also* observed. DOX molecules generally intertwine with the polymer chains through various interactions forming compact particles.[21] With increasing polymer chains the amount of interactions increase bringing the constructs closer together, evidently decreasing the overall diameter of the complex. The zeta potential of the nanocomplexes with increasing complexation ratios (from 6.25 to 1250) exhibited an overall negative charge. A slight decrease in the zeta potential was observed in the system which was attributed to the enhancement of anionic carboxyl groups of the polymer chains in the final nanocomplex.

Table 1 Mean hydrodynamic diameter, polydispersity index (PDI), and ζ-potential of P(MAA-*co*-CMA)–DOX nanocomplexes containing 50 μM DOX at varying complexation ratios

P(MAA-*co*-CMA)–DOX nanocomplex	Diameter (nm)	PDI	ζ-Potential (mV)
6.25 : 1	113.5 ± 14.2	0.47 ± 0.07	−20.7 ± 1.2
125 : 1	109.4 ± 17.3	0.47 ± 0.02	−23.5 ± 3.1
1250 : 1	62.9 ± 6.3	0.45 ± 0.06	−29.8 ± 0.5

Toxicity screening of P(MAA-*co*-CMA)–DOX nanocomplexes

The toxicity profiles of P(MAA-*co*-CMA)–DOX nanocomplexes (at 125 : 1 and 1250 : 1 conjugation ratios) in comparison to free DOX treatments were evaluated in SHEP, HepG2 and MRC5 cells at 72 hours. Previous cell toxicity studies conducted with P(MAA-*co*-CMA) copolymer series demonstrated high levels of viability, between concentrations of 0.05 μM and 50 μM, in the designated cell lines.[53] The half-maximal inhibitory concentration (IC_{50}) doses of the polymers were not calculated due to their exceptionally low toxicity values. The variance of CMA ratio in the copolymer compositions, did not exhibit any major differences in toxicity amongst each other, as polymers or as nanocomplexes (Fig. S4 and S5, ESI†).

The IC_{50} values of each nanocomplex in each cell line are represented in Table 2. The MRC5 IC_{50} values were 2.4-fold higher for free DOX and between 8-fold (125 : 1) and 12.5-fold (1250 : 1) higher in the case of P(MAA-*co*-CMA)–DOX nanocomplexes than those for SHEP cells.

Conversely, the SHEP IC_{50} values of free DOX treatments were 3.3-fold higher than the P(MAA-*co*-CMA)–DOX nano-

 This journal is © The Royal Society of Chemistry 2015

Published on 25 September 2014. Downloaded by Izmir Yuksek Teknoloji on 22/05/2017 11:50:19.

Table 2 IC_{50} values (μM) of DOX and P(MAA-*co*-CMA)–DOX nanocomplexes in various cell lines[a]

Nanocomplex ratios		SHEP	HepG2	MRC5
DOX		0.36 ± 0.141	0.93 ± 0.014	0.87 ± 0.139
2 mol% CMA-DOX	125 : 1	0.11 ± 0.006*	0.82 ± 0.135	0.78 ± 0.029
	1250 : 1	0.10 ± 0.002*	0.77 ± 0.100	0.90 ± 0.044
4 mol% CMA-DOX	125 : 1	0.11 ± 0.004*	0.90 ± 0.148	0.82 ± 0.058
	1250 : 1	0.10 ± 0.006*	1.77 ± 0.351	1.70 ± 0.183**
8 mol% CMA-DOX	125 : 1	0.12 ± 0.004*	0.82 ± 0.028	0.71 ± 0.056
	1250 : 1	0.12 ± 0.008*	3.07 ± 0.238	1.50 ± 0.367*

[a] IC_{50} values for *P(MAA-*co*-CMA)–DOX treatments (both 125 : 1 and 1250 : 1) in SHEP cells were significantly less than DOX. The significance between IC_{50} values for P(MAA–*co*-CMA)-DOX treatments in HepG2 cells were DOX *vs.* 4 mol% CMA-DOX (**), DOX *vs.* 8 mol% CMA-DOX (***), 2 mol% CMA-DOX *vs.* 4 mol% CMA-DOX (**), 2 mol% CMA-DOX *vs.* 8 mol% CMA-DOX (***) and 4 mol% CMA-DOX *vs.* 8 mol% CMA-DOX (***). IC_{50} values of **4 mol% CMA-DOX and *8 mol% CMA-DOX at 1250 : 1 were significantly greater than both DOX and 2 mol% CMA-DOX in MRC5 cells. IC_{50} values were calculated in graph pad prism *via* nonlinear regression analysis. One way Anova with Tukeys multiple comparisons follow up tests for significance.

complexes at both 125 : 1 and 1250 : 1 conjugation ratios, indicating that P(MAA-*co*-CMA)–DOX nanocomplexes are more efficient than free DOX in SHEP cells. HepG2 cells demonstrated a similar trend where the IC_{50} value of free DOX was slightly higher than nanocomplexes (125 : 1 and 1250 : 1), however showed some fluctuations with nanocomplex samples of 4 mol% CMA and 8 mol% CMA prepared at 1250 : 1 ratio. This increase can be attributed to the uptake mechanism of the polymers in HepG2 cells. Internalization *via* CIE where endo/lysosomal trafficking is hindered due to the absence of caveosomes – the signal between cellular compartments –[54] may lead to the entrapment of complexes in cell vesicles.[55] The high anionic character of the complexes overpowers the membrane destabilizing properties of the polymer thus resulting in engulfed particles incapable of reaching the target site, nucleus.[56]

It should be mentioned that HepG2 cells were less susceptible to DOX related treatments owing to their slow growth rate[57] which is not favourable in the case of DOX internalization. In line with previous reports,[58,59] the data suggests that P(MAA-*co*-CMA)–DOX nanocomplexes demonstrate greater efficacy than free DOX samples in carcinoma cell lines and exhibit lesser toxicity in normal cells.

Intracellular uptake of P(MAA-*co*-CMA)–DOX nanocomplexes

FLIM was employed to characterize uptake of P(MAA-*co*-CMA)–DOX nanocomplexes (at 125 : 1 w/w ratio) in live cells. FLIM images, captured at 1 and 4 hour time-points, displayed two-different lifetimes in SHEP cells which were associated with free and conjugated DOX.

The phasor region, associated with P(MAA-*co*-CMA)–DOX nanocomplexes in solution (highlighted by the yellow cursor) represents the longer fluorescence lifetime species. The fluorescence lifetime of the complexes, indicated in yellow, are shown in the region images pinpointing the exact location of the complexes in the cell (Fig. 6). The shortest lifetime species is represented by the green cursor, with this being associated with free DOX residing in the nucleus and a longer lifetime species in the cytoplasm as represented by red pixels as selected with the red cursor in the phasor plot. In the first 4 hours, both P(MAA-*co*-CMA)–DOX nanocomplexes and cleaved DOX are present in the cells, where overtime the released DOX localizes in the nucleus with increasing concentrations. In contrast, P(MAA-*co*-CMA)–DOX nanocomplexes begin accumulating in the cytoplasm with increasing time. The shorter fluorescence lifetime becoming more dominant overtime indicates that DOX is in fact being effectively released from the P(MAA-*co*-CMA)–DOX nanocomplexes following their cellular uptake in a time-dependent manner.[50,60]

Confocal laser scanning microscopy was conducted to visualize cellular uptake of the P(MAA-*co*-CMA)–DOX nanocomplexes in SHEP, HepG2 and MRC5 cell lines as function of time. Nanocomplexes, comprising DOX and P(MAA-*co*-CMA) were prepared at two conjugation ratios (125 : 1 and 1250 : 1) and incubated for 1, 4 and 24 hours prior to imaging. The cell nuclei were stained with 5 μg ml^{-1} Hoechst 33342. Free DOX treatments were included merely as control images.

Fig. 7 shows the cellular internalization of nanocomplexes in SHEP cells over time. Images suggest that complexes are readily up taken and start localizing in nucleus by 4 hours,

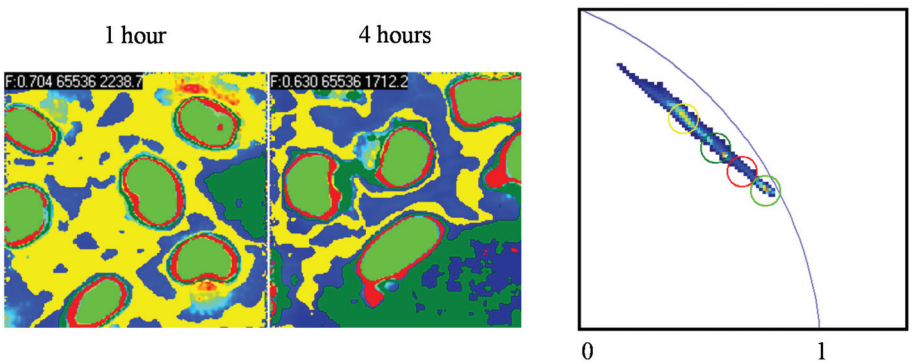

Fig. 6 Region of interest (ROI) examined and the corresponding phasor plot of free DOX and P(MAA-*co*-CMA)–DOX nanocomplexes at 125 : 1 w/w ratio after 1 hour and 4 hours in SHEP cells.

Published on 25 September 2014. Downloaded by Izmir Yuksek Teknoloji on 22/05/2017 11:50:19.

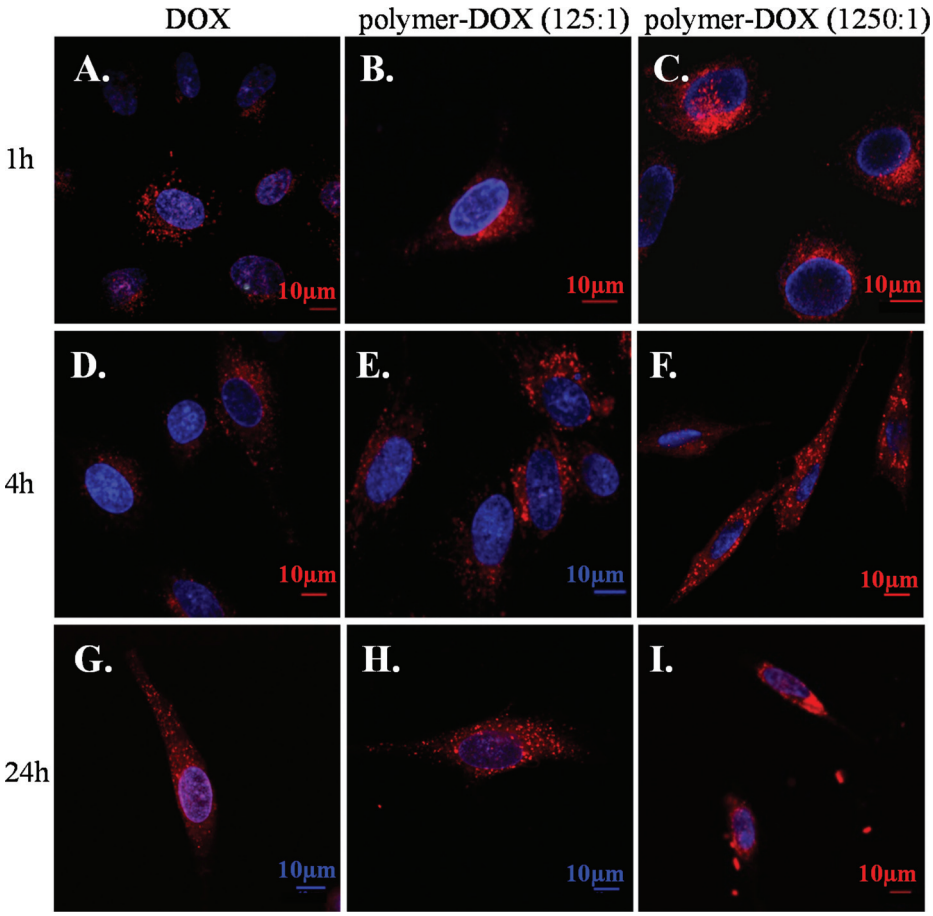

Fig. 7 Confocal laser scanning microscopy exhibiting cellular internalization of 0.5 μM DOX and P(MAA-*co*-CMA)–DOX nanocomplexes at conjugation ratios of 125 : 1 and 1250 : 1 within (A–C) 1 hour, (D–F) 4 hours and (G–I) 24 hours in SHEP cells. Nuclei (represented in blue) were visualized with Hoechst 33342 stain. DOX fluorescent images were acquired at λ^{ex} = 485 nm and λ^{em} = 595 nm (visualized in red). Scale bars are used to indicate 10 μm.

while by 24 hours, complexes have broken down further (in line with FLIM stability data) with a large amount of DOX localized to the nucleus. Complexes formed with higher polymer ratio (1250 : 1) presented similar cellular internalization results at 1 and 4 hours; however at 24 hours viability of the cells was drastically reduced owing to the high polymer content.

Fig. S6 displays the nanocomplex uptake at 1, 4 and 24 hour intervals in HepG2 cells. In agreement with toxicity profiles, HepG2 cells are less susceptible to internalization of P(MAA-*co*-CMA)–DOX nanocomplexes. This could be attributed to the difference in internalization mechanism/properties like rate of nutrient uptake, doubling time and other biochemical processes between cell lines.[56,61,62] The slower growth rate of HepG2[57] drives complexes at 125 : 1 to internalize and release the majority of their load after 4 hours and with nuclear localization visible at 24 hours. Alexa Fluor 488 labelled polymers were used to verify the complexation between the two components and visualize complex localized DOX release at 4 hours (Fig. S6-E, ESI†).

Finally the complex uptake profile was investigated in MRC5 cells lines over the course of 1 and 4 hours (Fig. S7, ESI†). Complex treatments showed similar uptake patterns at same time points attaining the load mostly in the cytoplasm instead of it target site, nucleus.

The endocytic profile of P(MAA-*co*-CMA)–DOX nanocomplexes

Flow cytometry was employed to investigate the specific endocytic pathway of the P(MAA-*co*-CMA)–DOX nanocomplexes prepared at 1250 : 1 (w/w) ratio in SHEP an HepG2 cell lines. A representative confocal imaging study of SHEP cells investigating the endocytic profile of nanocomplexes can be seen in Fig. S8, ESI.† Cells were treated with nanocomplexes in the presence of the pharmacological inhibitors – genistein, chlorpromazine and MβCD – to block CDE and CIE pathways.[9] Fig. 8 illustrates the cellular inhibition of nanocomplex uptake as detected from the fluorescence intensity of DOX. A control set, evaluating free DOX uptake in the presence of inhibitors, resulted in no inhibitory effects which is due to the fact that the cellular uptake process of DOX is governed by passive diffusion rather than endocytosis (data not included).[63,64] The endocytic pathway of the P(MAA-*co*-CMA) copolymers alone were shown to be CIE due to the cholesterol units in their polymer-chain; while the nanocomplexes demonstrated altered mechanisms of uptake which could be attributed to the

 This journal is © The Royal Society of Chemistry 2015

Published on 25 September 2014. Downloaded by Izmir Yuksek Teknoloji on 22/05/2017 11:50:19.

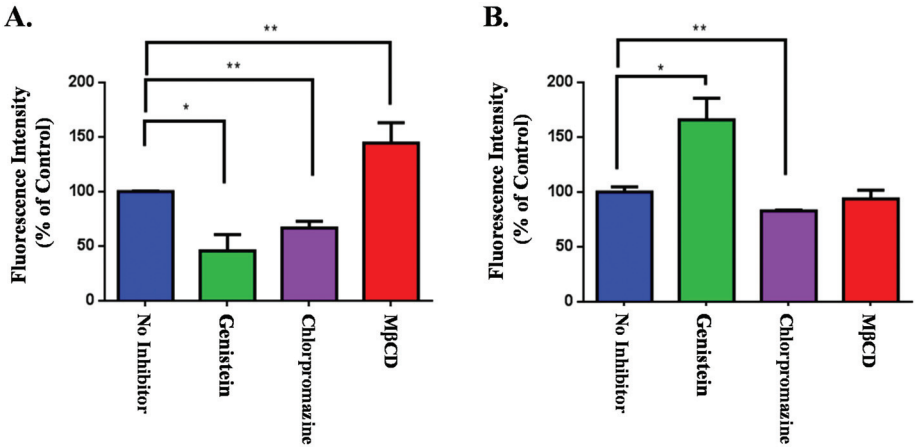

Fig. 8 Inhibition of P(MAA-*co*-CMA)–DOX nanocomplexes after incubation with endocytic inhibitors (300 μM genistein, 5 μg ml^{-1} chlorpromazine and 2.5 mM MβCD for 2 hours) in (A) SHEP and (B) HepG2 cells determined by Flow Cytometry.

change in size, charge density, and self-assembly that occurred with DOX complexation.

The efficacy of endocytic inhibitors are known to drastically differ between cell lines.[56,65] The variance between SHEP and HepG2 cells metabolism, growth rate and cell morphologies cause these inhibitors to display different expression profiles. The pre-treatment of genistein, a tyrosine kinase inhibitor that disrupts the actin network of and cells and inhibits dynamin II the master regulator of membrane trafficking,[66] demonstrated contrasting uptake profiles for both cell lines. The rearrangement of the actin cytoskeleton and disruption of ligand triggered uptake in SHEP cells decreased the cellular internalization profile of P(MAA-*co*-CMA)–DOX nanocomplexes by 54.4%. This inhibition profile suggests that nanocomplexes take a ligand triggered caveolae-mediated route while internalizing in to SHEP cells. Owing to the slower metabolic rate of HepG2 cells neither the internalization rate – as seen in toxicity and microscopy studies – nor the inhibition profile of nanocomplexes in SHEP cells are the same. It can be speculated that the delay in rearranging the actin network of HepG2 cells may have caused leakiness in membrane surface thus allowing nanocomplexes to be taken up through diffusion rather than endocytosis. No significant inhibition data was detected with MβCD treatments hinting nanocomplexes to favour either CIE or CDE mechanisms in both cells. The CDE pathway was investigated through chlorpromazine treatments, where the internalization of nanocomplexes was significantly reduced by 33.4% and 17.4% in SHEP and HepG2 cells, respectively.

The whole data suggests that both CDE and caveolae-mediated mechanisms influence the uptake of P(MAA-*co*-CMA)–DOX nanocomplexes in SHEP cells, with caveolae-mediated endocytosis contributing to cellular internalization to a greater degree. This is a common occurrence with pharmacological endocytic pathway inhibition; in the event of blocking one pathway cells are able to adapt and up-regulate by another internalization mechanism,[8,32,36] and *in our case* demonstrate multiple endocytic pathways.[8,67,68] Caveolae-mediated endocytosis, the dominant uptake mechanism, was strongly influenced by both hydrophobic interactions and size effects.[11] While cholesterol moieties on polymer chains governed interactions with glycosphingolipid rich microdomains on the plasma membrane, the average nanocomplex diameter (62 nm at 1250 : 1 ratio) coincided with the size of caveolae invaginations in the cell membrane (50–80 nm) thus evidencing caveosomes as the primary endocytic mechanism.[32,69]

Overall, caveolae-mediated endocytosis is the principle pathway for P(MAA-*co*-CMA) internalization which has the potential to override the mechanisms involved in P(MAA-*co*-CMA)–DOX nanocomplex cellular uptake (as it showed higher inhibition profile). The caveolae-mediated endocytosis process offers a significant advantage of transcytosing its load across the cells efficiently with the potential of enhancing deep tissue and vascular penetration of its cargo drugs.[8,70]

Experimental

Materials

The synthesis of cholesterol methacrylate (CMA) and the RAFT polymerization of P(MAA-*co*-CMA) copolymer series (2 mol% CMA, cholesterol content 2 mol%, with number average molecular weight $(M_n)_{GPC}$ of 16 500 g mol^{-1} and polydispersity index (PDI) of 1.19; 4 mol% CMA, cholesterol content 4 mol%, with $(M_n)_{GPC}$ 15 800 g mol^{-1} and PDI 1.10; 8 mol% CMA, cholesterol content 8 mol%, with $(M_n)_{GPC}$ 18 000 g mol^{-1} and PDI 1.11) have been previously described.[31,71] DBL® Doxorubicin hydrochloride (DOX) and *N*-hydroxysulfosuccinimide (NHS-sulfo) were obtained from Hospira Australia Pty Ltd and Thermo Scientific, respectively. Ethyl (dimethylaminopropyl) carbodiimide (EDC), tris(2-carboxyethyl) phosphine (TCEP), cystamine dihydrochloride, phosphate buffered saline (PBS), poly-D-lysine hydrobromide, bisBenzimide H 33342 trihydrochloride (Hoechst 33342), genistein, methyl-β-cyclodextrin and chlorpromazine hydrochloride were purchased from Sigma-Aldrich. Dulbecco's Modified Eagle Medium (DMEM)

Published on 25 September 2014. Downloaded by Izmir Yuksek Teknoloji on 22/05/2017 11:50:19.

with 4.5 g L^{-1} glucose and L-glutamine, heat inactivated Foetal Calf Serum (FCS), trypsin solution (0.25% (w/v) trypsin in Hank's solution), Trypan Blue and OptiMEM® I Reduced Serum Medium were obtained from Invitrogen Life Technologies. Transferrin from human serum AlexaFlour®647 conjugate, BODIPY® FLC5-lactosylceramide complexed to BSA and Alexa Fluor® 488 maleimide dye were purchased from Invitrogen Molecular Probes™.

Instruments

Fourier transform infrared spectrometer. Attenuated Total Reflection-Fourier Transform Infrared Spectroscopy (ATR-FTIR) measurement was obtained by a Bruker IFS66/S High End FT-NIR/IR Spectrometer system using diffuse reflectance sampling accessories and a resolution of 4 cm^{-1}. The spectrum for the copolymer was recorded in the region of 500 to 5000 cm^{-1} using 256 scans.

UV-Visible spectrophotometer. UV-Visible (UV-Vis) spectra were obtained by a double beam Hitachi – UV spectrometer (Model no: U-2800) using UV solutions 2.1 software. The instrument was equipped with a double beam light source carrying a detection range from 190 nm to 1100 nm and a photometric range of 5 absorbance units. The absorbance of copolymer solutions were measured at 400 nm while P(MAA-*co*-CMA)–DOX nanocomplexes were analysed at 485 nm using quartz cuvettes.

Dynamic light scattering. Dynamic light scattering (DLS) studies and ζ-potential measurements were performed using a Malvern Zetasizer NaNo ZS Instrument (Malvern, USA) equipped with a 4 mV He–Ne laser operating at λ = 633 nm, an avalanche photodiode detector with high quantum efficiency, and an ALV/LSE-5003 multiple tau digital correlator electronics system. Size measurements were performed in Disposable Solvent Resistant Micro Cuvettes ZEN0040 (Malvern Instruments) recorded in nanometres (nm) while charge readings were conducted in Folded Capillary Cells DTS1060 (Malvern Instruments) shown in millivolts (mV). The dispersant parameters used for the analyses were RI: 1.330, Abs: 0.01 and diluent (water) viscosity: 0.88 cP. The P(MAA-*co*-CMA)–DOX sample solutions were prepared in MilliQ water with a fixed DOX concentration of 50 μM at varying complexation ratios. All samples were measured by scanning 7 times with each time of automatic measurement. Assays were done in duplicates.

Flow cytometer. Falcon 5 mL polystyrene round bottom tubes (12 mm × 75 mm) were used for cell collection and purchased from Becton Dickinson. A FACSCanto™ flow cytometer (Becton-Dickinson) equipped with BD Biosciences FACSDiva Software was used for cell cycle analysis. The flow rate was <200 nuclei and 10 000 cells for each sample were analyzed. The CellQuest program was used to quantitate the distribution of cells in each cell cycle phase.

Fluorescence lifetime imaging microscopy. Fluorescence lifetime imaging (FLIM) was performed on a Microtime200 inverted confocal microscope (PicoQuant GmbH) equipped with a 60 × 1.2 NA water-immersion objective and a field-of-view area of 80 × 80 microns. Excitation was achieved by a fiber-coupled picosecond-pulsed, variable-repetition-rate diode laser operating at 470 nm with a pulse width below 200 ps. The emission was collected using a 550 nm long-pass filter and a single-photon avalanche diode (SPAD) (PDM, MicroPhoton Devices) coupled to time-correlated single-photon counting (TCSPC) electronics (Picoharp300, PicoQuant). SymphoTime Software (PicoQuant) was utilized for data acquisition. The SIMFCS Software, which was developed at the Laboratory for Fluorescence Dynamics (University of California), was employed for phasor analysis of the attained FLIM data.

Methods

Fluorescent labelling of P(MAA-*co*-CMA) copolymers. 2 mol% of the carboxylic acid groups on each P(MAA-*co*-CMA) sample was targeted and modified according to the protocol described in literature.[25] A model calculation for polymer modifications and labelling is as follows: Purified 8 mol% CMA (5 mg, 32.7 μmol carboxylate groups) was dissolved in 1 mL buffer (0.1 M sodium phosphate buffer, pH 7.5), yielding a polymer solution of 0.30 mM. The polymer was reacted with 2-fold molar excess of EDC/NHS-sulfo (0.62 μmol/1.62 μmol) at room temperature for 15 minutes. The pH of the reaction mixture was adjusted to 7.0 then supplemented with 10-fold molar excess of cystamine dihydrochloride (30 mM). The reaction continued in room temperature for 2 hours at pH 7.0. Upon completion the polymer was purified by dialysis (against MilliQ water) for 2 days. The product was freeze dried and analysed *via* FTIR.

ATR-FTIR (cm^{-1}) for 8 mol% CMA: 3400–2900 (carboxylic acid O–H stretching), 3100–2700 (alkene and alkane C–H stretching), 1735–1650 (C═O ester stretching), 1630–1550 (carboxyl anions C═O stretching), 1170 (C–O–C stretching), 900–644 (aromatic C–H bending).

ATR-FTIR (cm^{-1}) for 8 mol% CMA-modified: 3400–2900 (carboxylic acid O–H stretching), 3100–2700 (alkene and alkane C–H stretching), 1735–1650 (C═O ester stretching), 1650–1580 (N–H bend), 1020–1220 (aliphatic amines), 1160 (C–O–C stretching), 900–644 (aromatic C–H bending) (Fig. 1-A).

0.5 mg of the modified polymer was dissolved in 50 μL phosphate buffer solution (pH 7.8). 14 μL of Alexa Fluor® 488, a fluorescent maleimide dye, (stock solution 20 mM) was included to the polymer solution resulting in a 4-fold molar excess to thiol-reactive groups. At the beginning of the reaction 15 mg of tris(2-carboxyethyl) phosphine (TCEP) (15-fold excess) was dissolved into this mixture to reduce the disulphide bonds of cystamine dihydrochloride. 2 hours later another 15 mg of TCEP was supplemented to the mixture allowing the reaction to proceed for an additional 3 hours. The product was purified by dialysis (against MilliQ water) in the dark for 3 days. In line with previous detection studies,[72] UV-Vis investigations of P(MAA-*co*-CMA) copolymers revealed a distinctive peak at 275 nm, which enhanced with increasing CMA moieties, evidencing the short wavelength to be specific to cholesterol units in the composition. Accordingly the fluo-

 This journal is © The Royal Society of Chemistry 2015

Published on 25 September 2014. Downloaded by Izmir Yuksek Teknoloji on 22/05/2017 11:50:19.

rescent dye content of 8 mol% CMA was quantified by UV-Vis spectrometer analysis, where a calibration curve was built from standard solutions of 8 mol% CMA in MilliQ water at 275 nm (Fig. 1-B).

Preparation and characterization of P(MAA-*co*-CMA)–DOX nanocomplexes. DOX was dissolved in MilliQ water at a final concentration of 0.8 μg ml^{-1}. P(MAA-*co*-CMA) copolymer solutions, prepared in MilliQ water, were added to the DOX solution at equal volume to form final complex (P(MAA-*co*-CMA)–DOX) ratios of 1 : 1, 6.25 : 1, 12.5 : 1, 62.5 : 1, 125 : 1, 625 : 1, 1250 : 1, and 6250 : 1 w/w. Owing to the strong electrostatic interaction a 5 minute complexation period in the dark resulted in instant complexation. Nanocomplex formation was analysed by FLIM and UV-Vis Spectroscopy. The hydrodynamic mean diameter and zeta potential of the P(MAA-*co*-CMA)–DOX nanocomplexes was measured by DLS at a wavelength of 633 nm with a 90° detection angle at 25 °C.

Toxicity screening of P(MAA-*co*-CMA)–DOX nanocomplexes. The toxicity profile of free DOX and P(MAA-*co*-CMA)–DOX nanocomplexes was evaluated in human neuroblastoma SHEP cells, human liver hepatocellular carcinoma (HepG2) cells and human foetal lung fibroblast MRC5 cells by an Alamar Blue[73] assay. Cells were seeded in 96-well flat-bottom plates at concentrations of 5×10^3 cells per well for SHEP, 10×10^3 cells per well for HepG2 and 5×10^3 cells per well for MRC5 and incubated at 37 °C in 5% CO_2 and 95% humidity for 24 hours. After surface adherence, cells were treated with free DOX and nanocomplexes – at 2 different complexation (w/w) ratios – over an equivalent DOX concentration range of 0.005 μM–5 μM for 72 hours. Following the incubation period, treatments were removed and replaced with 100 μL fresh media and 20 μL of Alamar Blue per well and further incubated for another 6 hours. Cell viability was assessed by comparing treated cells to positive control cells (100% viability).

Fluorescence microscopy imaging. Cells (5000–7000 cells per dish) were plated in 35 mm cultured dishes which were pre-coated with poly-D-lysine hydrobromide for 5 minutes. After 72 hours of surface adherence, cells were transfected with P(MAA-*co*-CMA)–DOX conjugates – at various complexation ratios – for 1, 4 and/or 24 hours. Transfected cells were rinsed with PBS and then stained with a nuclear dye (5 μg ml^{-1} bisBenzimide H 33342 trihydrochloride (Hoechst 33342)) for 5 minutes. An inverted confocal laser scanning microscope; Zeiss LSM 780, equipped with an environmental chamber which controls the atmospheric conditions, humidity and temperature, was utilized for capturing live-cell images. The confocal microscope was fitted with a 63× 1.4 NA water objective that included multiple laser lines (405, 458, 488, 514, 561, and 633 nm) for fluorescence measurements.

Statistical analysis. Single factor analysis of variance (ANOVA) with a Tukeys multiple comparison follow up was employed for statistical analysis of comparative data. Results were expressed as means of at least three independent experiments ± SD where $*P < 0.05$, $**P < 0.01$, $***P < 0.005$ values were considered statistically significant.

Conclusions

In conclusion, P(MAA-*co*-CMA) copolymer series, with varying cholesterol units, were evaluated for their endocytic profile and therapeutic efficiency. P(MAA-*co*-CMA) copolymers were modified *via* EDC/NHS-sulfo reactions and fluorescently labelled with Alexa Fluor® 488 for imaging and endocytic inhibition studies. The cellular internalization pathway of P(MAA-*co*-CMA) copolymers was discovered to be clathrin-independent endocytosis (caveolae mediated and cholesterol dependent endocytosis) in both SHEP and HepG2 cell lines. Initial characterization *via* FLIM, UV-Vis and DLS verified the ionic complexation between P(MAA-*co*-CMA)–DOX nanocomplexes at varying w/w ratios. The nanocomplexes showed a more pronounced cytotoxicity in SHEP cells in comparison to HepG2 and MRC5 cells while displaying 3.3-fold lower IC_{50} values than free-DOX treatments. The cellular uptake profile of P(MAA-*co*-CMA)–DOX nanocomplexes, investigated *via* FLIM and confocal microscopy, showed DOX accumulation in the nucleus over time. Endocytic inhibition studies were performed to discover the specific uptake mechanism of the nanocomplexes. Flow cytometry and confocal microscopy results indicated the nanocomplexes to be involved in multiple endocytic pathways with caveolae-mediated uptake being the dominant mechanism in SHEP cells. The therapeutic profile of P(MAA-*co*-CMA) copolymers, reported herein, indicates that these nano-sized constructs are suited to drug delivery applications and further polymer modifications could enhance their efficacy in *in vivo* treatments.

Acknowledgements

MK is supported by an NHMRC Senior Research Fellowship (APP1058299). The authors thank the Nuclear Magnetic Resonance Facility, Biomedical Imaging Facility and the Electron Microscope Unit at the Mark Wainwright Analytical Centre, University of New South Wales.

References

1 K. Osada, R. J. Christie and K. Kataoka, *J. R. Soc., Interface*, 2009, **6**, S325–S339.
2 M. C. Jones and J. C. Leroux, *Eur. J. Pharm. Biopharm.*, 1999, **48**, 101–111.
3 A. V. Kabanov, P. Lemieux, S. Vinogradov and V. Alakhov, *Adv. Drug Delivery Rev.*, 2002, **54**, 223–233.
4 A. Lavasanifar, J. Samuel and G. S. Kwon, *Adv. Drug Delivery Rev.*, 2002, **54**, 169–190.
5 V. P. Torchilin, *J. Controlled Release*, 2001, **73**, 137–172.
6 R. Duncan, *Nat. Rev. Drug Discovery*, 2003, **2**, 347–360.
7 S. Zhu, M. Hong, L. Zhang, G. Tang, Y. Jiang and Y. Pei, *Pharm. Res.*, 2010, **27**, 161–174.
8 P. M. McLendon, K. M. Fichter and T. M. Reineke, *Mol. Pharmaceutics*, 2010, **7**, 738–750.

Published on 25 September 2014. Downloaded by Izmir Yuksek Teknoloji on 22/05/2017 11:50:19.

9 I. A. Khalil, K. Kogure, H. Akita and H. Harashima, *Pharmacol. Rev.*, 2006, **58**, 32–45.
10 D. Vercauteren, R. E. Vandenbroucke, A. T. Jones, J. Rejman, J. Demeester, S. C. De Smedt, N. N. Sanders and K. Braeckmans, *Mol. Ther.*, 2010, **18**, 561.
11 X. Zeng, Y. Zhang and A. M. Nyström, *Biomacromolecules*, 2012, **13**, 3814–3822.
12 A. Aderem and D. M. Underhill, *Annu. Rev. Immunol.*, 1999, **17**, 593–623.
13 J. Liu, H. Bauer, J. Callahan, P. Kopečková, H. Pan and J. Kopeček, *J. Controlled Release*, 2010, **143**, 71–79.
14 L. A. Bareford and P. W. Swaan, *Adv. Drug Delivery Rev.*, 2007, **59**, 748–758.
15 J. Harris, D. Werling, J. C. Hope, G. Taylor and C. J. Howard, *Trends Immunol.*, 2002, **23**, 158–164.
16 W. J. Hoskins, C. A. Perez, R. C. Young, R. R. Barakat and M. Markman, *Principles and Practice of Gynecologic Oncology*, Lippincott Williams & Wilkins, 2005.
17 J. G. Zijlstra, E. G. E. de Vries and N. H. Mulder, *Cancer Res.*, 1987, **47**, 1780–1784.
18 T. Ehtezazi, T. Govender and S. Stolnik, *Pharm. Res.*, 2000, **17**, 871–877.
19 T. Bogush, G. Smirnova, I. Shubina, A. Syrkin and J. Robert, *Cancer Chemother. Pharmacol.*, 1995, **35**, 501–505.
20 M. V. Kitaeva, N. S. Melik-Nubarov, F. M. Menger and A. A. Yaroslavov, *Langmuir*, 2004, **20**, 6575–6579.
21 Y. Tian, P. Ravi, L. Bromberg, T. A. Hatton and K. C. Tam, *Langmuir*, 2007, **23**, 2638–2646.
22 B. Manocha and A. Margaritis, *J. Nanomater.*, 2010, 2010.
23 I. Oh, K. Lee, H.-Y. Kwon, Y.-B. Lee, S.-C. Shin, C.-S. Cho and C.-K. Kim, *Int. J. Pharm.*, 1999, **181**, 107–115.
24 G. S. Kwon and M. L. Forrest, *Drug Dev. Res.*, 2006, **67**, 15–22.
25 G. T. Hermanson, *Bioconjugate Techniques*, Copyright © 2008 Elsevier Inc., 2008.
26 M.-A. Yessine, C. Meier, H.-U. Petereit and J.-C. Leroux, *Eur. J. Pharm. Biopharm.*, 2006, **63**, 1–10.
27 A. Akinc, M. Goldberg, J. Qin, J. R. Dorkin, C. Gamba-Vitalo, M. Maier, K. N. Jayaprakash, M. Jayaraman, K. G. Rajeev, M. Manoharan, V. Koteliansky, I. Rohl, E. S. Leshchiner, R. Langer and D. G. Anderson, *Mol. Ther.*, 2009, **17**, 872–879.
28 D. V. Morrissey, J. A. Lockridge, L. Shaw, K. Blanchard, K. Jensen, W. Breen, K. Hartsough, L. Machemer, S. Radka, V. Jadhav, N. Vaish, S. Zinnen, C. Vargeese, K. Bowman, C. S. Shaffer, L. B. Jeffs, A. Judge, I. MacLachlan and B. Polisky, *Nat. Biotechnol.*, 2005, **23**, 1002–1007.
29 S. Zhang, Y. Xu, B. Wang, W. Qiao, D. Liu and Z. Li, *J. Controlled Release*, 2004, **100**, 165–180.
30 J. Soutschek, A. Akinc, B. Bramlage, K. Charisse, R. Constien, M. Donoghue, S. Elbashir, A. Geick, P. Hadwiger, J. Harborth, M. John, V. Kesavan, G. Lavine, R. K. Pandey, T. Racie, K. G. Rajeev, I. Rohl, I. Toudjarska, G. Wang, S. Wuschko, D. Bumcrot, V. Koteliansky, S. Limmer, M. Manoharan and H.-P. Vornlocher, *Nature*, 2004, **432**, 173–178.
31 S. Sevimli, F. Inci, H. M. Zareie and V. Bulmus, *Biomacromolecules*, 2012, **13**, 3064–3075.
32 S. D. Conner and S. L. Schmid, *Nature*, 2003, **422**, 37–44.
33 M. Kaksonen, C. P. Toret and D. G. Drubin, *Nat. Rev. Mol. Cell Biol.*, 2006, **7**, 404–414.
34 L.-H. Wang, K. G. Rothberg and R. G. W. Anderson, *J. Cell Biol.*, 1993, **123**, 1107–1117.
35 S. K. Rodal, G. Skretting, Ø. Garred, F. Vilhardt, B. van Deurs and K. Sandvig, *Mol. Biol. Cell*, 1999, **10**, 961–974.
36 S. M. Uriarte, N. R. Jog, G. C. Luerman, S. Bhimani, R. A. Ward and K. R. McLeish, *Am. J. Physiol.: Cell Physiol.*, 2009, **296**, C857–C867.
37 I. R. Nabi and P. U. Le, *J. Cell Biol.*, 2003, **161**, 673–677.
38 A. Widera, F. Norouziyan and W. C. Shen, *Adv. Drug Delivery Rev.*, 2003, **55**, 1439–1466.
39 J. Rejman, V. Oberle, I. S. Zuhorn and D. Hoekstra, *Biochem. J.*, 2004, **377**, 159–169.
40 I. S. Zuhorn, R. Kalicharan and D. Hoekstra, *J. Biol. Chem.*, 2002, **277**, 18021–18028.
41 M. Vrljic, S. Y. Nishimura, W. E. Moerner and H. M. McConnell, *Biophys. J.*, 2005, **88**, 334–347.
42 S. A. Francis, J. M. Kelly, J. McCormack, R. A. Rogers, J. Lai, E. E. Schneeberger and R. D. Lynch, *Eur. J. Cell Biol.*, 1999, **78**, 473–484.
43 M. V. Kitaeva, N. S. Melik-Nubarov, F. M. Menger and A. A. Yaroslavov, *Langmuir*, 2004, **20**, 6796–6799.
44 P. R. Harrigan, K. F. Wong, T. E. Redelmeier, J. J. Wheeler and P. R. Cullis, *Biochim. Biophys. Acta, Biomembr.*, 1993, **1149**, 329–338.
45 B. Kim and Y. Shin, *J. Appl. Polym. Sci.*, 2007, **105**, 3656–3661.
46 X. Dai, Z. Yue, M. E. Eccleston, J. Swartling, N. K. H. Slater and C. F. Kaminski, *Nanomedicine*, 2008, **4**, 49–56.
47 D. M. Jameson, E. Gratton and R. D. Hall, *Appl. Spectrosc.*, 1984, **20**, 55–106.
48 M. A. Digman, V. R. Caiolfa, M. Zamai and E. Gratton, *Biophys. J.*, 2008, **94**, L14–L16.
49 O. Hovorka, V. Šubr, D. Větvička, L. Kovář, J. Strohalm, M. Strohalm, A. Benda, M. Hof, K. Ulbrich and B. Říhová, *Eur. J. Pharm. Biopharm.*, 2010, **76**, 514–524.
50 H. T. T. Duong, F. Hughes, S. Sagnella, M. Kavallaris, A. Macmillan, R. Whan, J. Hook, T. P. Davis and C. Boyer, *Mol. Pharmaceutics*, 2012, **9**, 3046–3061.
51 Y. Parisa, A. Fatemeh, F. E. Vashegani, S. Ramin and D. Rassoul, *Int. J. Nanomed.*, 2011, **6**, 1487–1496.
52 C. Peyratout, E. Donath and L. Daehne, *J. Photochem. Photobiol., A*, 2001, **142**, 51–57.
53 S. Sevimli, S. Sagnella, M. Kavallaris, V. Bulmus and T. P. Davis, *Biomacromolecules*, 2013, **14**, 4135–4149.
54 J. Rejman, A. Bragonzi and M. Conese, *Mol. Ther.*, 2005, **12**, 468–474.
55 C. Goncalves, E. Mennesson, R. Fuchs, J.-P. Gorvel, P. Midoux and C. Pichon, *Mol. Ther.*, 2004, **10**, 373–385.
56 K. L. Douglas, C. A. Piccirillo and M. Tabrizian, *Eur. J. Pharm. Biopharm.*, 2008, **68**, 676–687.

 This journal is © The Royal Society of Chemistry 2015

Published on 25 September 2014. Downloaded by Izmir Yuksek Teknoloji on 22/05/2017 11:50:19.

57 J. J. Centelles, A. Ramos-Montoya, S. Lim, S. Bassilian, L. G. Boros, S. Marin, M. Cascante and W.-N. P. Lee, *Metabolomics*, 2007, **3**, 105–111.
58 A. W. York, S. E. Kirkland and C. L. McCormick, *Adv. Drug Delivery Rev.*, 2008, **60**, 1018–1036.
59 K. Ulbrich and V. r. Šubr, *Adv. Drug Delivery Rev.*, 2004, **56**, 1023–1050.
60 S. M. Sagnella, H. Duong, A. MacMillan, C. Boyer, R. Whan, J. A. McCarroll, T. P. Davis and M. Kavallaris, *Biomacromolecules*, 2013, **15**, 262–275.
61 A. Kumar, V. K. Yellepeddi, G. E. Davies, K. B. Strychar and S. Palakurthi, *Int. J. Pharm.*, 2010, **392**, 294–303.
62 Y. Mo and L.-Y. Lim, *J. Pharm. Sci.*, 2004, **93**, 20–28.
63 M. Dalmark and H. H. Storm, *J. Gen. Physiol.*, 1981, **78**, 349–364.
64 M. Han, Y.-Y. Diao, H.-L. Jiang, X.-Y. Ying, D.-W. Chen, W.-Q. Liang and J.-Q. Gao, *Int. J. Pharm.*, 2011, **420**, 404–411.
65 P. Ilina, Z. Hyvonen, M. Saura, K. Sandvig, M. Yliperttula and M. Ruponen, *J. Controlled Release*, 2012, **163**, 385–395.
66 C.-J. Guo, D. Liu, Y.-Y. Wu, X.-B. Yang, L.-S. Yang, S. Mi, Y.-X. Huang, Y.-W. Luo, K.-T. Jia, Z.-Y. Liu, W.-J. Chen, S.-P. Weng, X.-Q. Yu and J.-G. He, *J. Virol.*, 2011, **85**, 6416–6426.
67 J. Contreras, A. Y. O. Elnagar, S. F. Hamm-Alvarez and J. A. Camarero, *J. Controlled Release*, 2011, **155**, 134–143.
68 F. Duchardt, M. Fotin-Mleczek, H. Schwarz, R. Fischer and R. Brock, *Traffic*, 2007, **8**, 848–866.
69 D. K. Sharma, J. C. Brown, A. Choudhury, T. E. Peterson, E. Holicky, D. L. Marks, R. Simari, R. G. Parton and R. E. Pagano, *Mol. Biol. Cell*, 2004, **15**, 3114–3122.
70 J.-S. Shin and S. N. Abraham, *Science*, 2001, **293**, 1447–1448.
71 X. Huang, S. Sevimli and V. Bulmus, *Eur. Polym. J.*, 2013, **49**, 2895–2905.
72 L. L. Smith, *Cholesterol Autoxidation*, Plenum, New York, 1981.
73 S. Sevimli, S. Sagnella, M. Kavallaris, V. Bulmus and T. P. Davis, *Polym. Chem.*, 2012, **3**, 2057–2069.